Macromolecules

pubs.acs.org/Macromolecules Article

Enhanced Ion Conductivity in a Poly(ionic liquid)-Grafted Nanoparticle-Based Single-Ion Conductor

Ruhao Li, Deniz Bulucu, Tsengming Chou, and Pinar Akcora*

Cite This: https://doi.org/10.1021/acs.macromol.3c02623 Read Online

ACCESS | Metrics & More | Article Recommendations | Supporting Information

ABSTRACT: In contemporary batteries, solid polymer electrolytes are widely prioritized for their easy processability and safety; however, they suffer from limited ionic conductivity. Polymerized ionic liquids (PILs) counter this shortcoming by combining mechanical properties of polyions while allowing the counterions (anions) to maintain their free mobility. Poly(1-vinylimidazolium bistriflimide)-grafted iron oxide (Fe_3O_4) nanoparticles with different chain lengths were synthesized to investigate the effect of grafting the PIL chains on the ionic conductivity. The long-range Coulombic interactions among PIL-grafted chains assist the formation of nanoparticle strings that percolate even at low particle concentrations. Within the percolated network, the connectivity of polycation grafts enabled effective ladder-like ion hopping of $TFSI^-$ anions and the cooperative ion motion in nanoparticle networks. The self-assembling nature of nanoparticles, when grafted with polymer electrolyte chains, increased ionic conductivity by promoting the facilitated transport of counterions. Upon incorporating ionic liquid to the PIL-grafted nanoparticles, the presence of ionic clustering was observed to decrease conductivity. Our results demonstrate that the graft chain confinement and particle percolation are essential factors for single-ion conductor design.

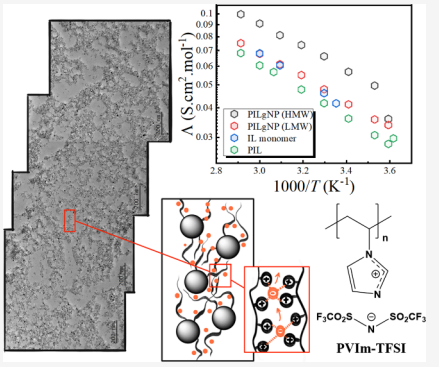

INTRODUCTION

In conventional electrolyte systems, the diffusivity differences of anions and cations lead to concentration gradients of ion carriers, limiting the performance of lithium-ion batteries. Single-ion conducting polymer electrolytes are highly promising conducting systems for energy applications.[1,2] The mobility of polymer backbone, glass transition temperature, and ion size impact the decoupling of ionic conductivity from segmental dynamics.[3−7] In addition, the ion solvation that is facilitated either by cosolvent addition or through preferential interactions between polymer chains and ions enhance the number of mobile (free) charge carriers.[8−12] In this study, the ion transport mechanism in ionic liquid (IL)-based polymer hybrids are investigated in solution and with the addition of IL. The underlying particle nanostructures and the polycation chain lengths are examined to explain the ion conductivity, which is unique for the single-ion conductor design.

ILs have been used as electrolytes in energy storage and conversion devices and in biomedicine owing to their unique advantages such as high ion density, negligible vapor pressure, nonflammability, and superior electrochemical and thermal stabilities,[13−15] which are essential for sustainability and eco-environmental safety.[16−25] Dynamics of ions is often described by the ion cage model (known as Coulombic cage), where ions are trapped within cages formed by neighboring ions, leading to subdiffusion at large length scales.[8,26−28] Extensive knowledge on structure and dynamics of ILs[29,30] empowers us to design materials based on polymerizable ionic liquids (PILs) with improved ion transport and mechanical properties. PILs are increasingly compelling as they exhibit good chemical and thermal stability, low glass transition temperature, and high charge density.[31] Additionally, these materials have been employed in wastewater purification and various membrane technologies.[32−34] The vinyl group-containing imidazolium-based ILs can be polymerized easily by atom transfer radical polymerization (ATRP) or reversible addition−fragmentation chain transfer (RAFT) polymerization.[35,36] Recent investigations on PILs have been carried out to examine the effect of counterion species (ion−ion correlations), molecular weight, polarizability, and dielectric constant for ion conduction.[6,28,37,38] However, the strong ion−ion correlations between polyions and counterions lower the number of charge carriers and suppress their ionic conductivity. We aim to address these issues by grafting the PIL chains on nanoparticles and expect that the conformation of grafted polyions will reduce ion−ion correlations and enhance their single-ion conductivity.

Intramolecular and intermolecular ion hopping by the formation and breaking of polyion−counterion associations was described as the *ladder mechanism* for ion transport in

Received: December 20, 2023
Revised: February 20, 2024
Accepted: March 12, 2024

PILs.[37−39] The ion associations involve one anion and four polymerized cationic monomers bonded to two polymer chains, and their average lifetimes determine the ion mobilities. Counter anions having a weak ion−ion correlation, e.g., bistriflimide ($TFSI^-$), bisfluorosulfonylimide (FSI^-), and hexafluorophosphate (PF_6^-), are preferred as they lead to shorter lifetimes of ion associations, hence the higher ion mobilities.[39] This work investigates the ion transport in PIL-grafted nanoparticle (PILgNP) solutions to demonstrate their potential as single-ion conductors, where polycations grafted on NPs, and their self-assembled network immobilizes the NPs. The percolation is essential for the movement of anions through polycation chains. In a previous work, the critical behavior of percolation was observed for poly(styrenesulfonate)-containing grafted NPs, manifested by an abrupt increase of ionic conductivity at the threshold concentration. The enhanced ionic conduction was attributed to the connectivity of telechelic sulfonated groups.[40]

Here, we present the impedance characteristics of the PILgNPs with different chain lengths at the same graft density and discuss ion transport mechanisms of the prepared systems in comparison to those of the free PIL homopolymer. The measured fast ion dynamics in PILgNPs is attributed to the confinement of counterions within the interstitial areas of particles and the polyion connection. The ion hopping following the ladder mechanism occurs fast[39] and results in even distribution[41] of anions along polycation chains. The enrichment of $TFSI^-$ within confined domains results in a chain-like cooperative ion motion where each anion moves a short distance, but an effective charge transport occurs over a long distance.[28] Additionally, the protic nature of 1-vinylimidazolium enables charge transfer through hydrogen bonding and breaking between neighboring imidazolium and imidazole pendants. NP self-assembly through polycation connectivity extends this mechanism to the micron scale. In summary, this work shows that the percolated network formed by PILgNPs enhances the charge transport over long distances, which has a substantial impact on the overall conductivity.

EXPERIMENTAL SECTION

Synthesis of VIm-TFSI. Monomeric 1-vinylimidazolium bistriflimide (VIm-TFSI) was synthesized by a quaternization reaction that occurs immediately upon mixing vinylimidazole (VIm) and bistriflimidic acid (HTFSI). Both chemicals were purchased from Fisher Scientific. The protocol was slightly modified from the previously reported procedures.[8,42] Due to the superacidity, deliquescence, and fuming of solid HTFSI, 0.4 g/mL HTFSI/acetonitrile (ACN) solution was prepared in a glovebox filled with argon.[43] The HTFSI/ACN solution was transferred from glovebox to chemical hood, and VIm was added dropwise to solution in an ice bath with vigorous magnetic stirring. The stoichiometric ratio of VIm to $TFSI^-$ was maintained at 1.05:1 to ensure complete reaction of HTFSI. The resulting mixture was then dried in vacuum for 12 h at room temperature, followed by additional drying at 60 °C for 12 h. A reported purification method utilizing 3 Å molecular sieves was adopted for removing moisture.[44] The product was stored in a desiccator with molecular sieves.

Polymerization of VIm-TFSI. VIm-TFSI was polymerized via the RAFT method with 4-cyano-4-(phenylcarbonothioylthio)-pentanoic acid (CPDB) as the chain transfer agent. Anchoring CPDB on 8 nm-diameter Fe_3O_4 NPs was previously reported.[40] Certain amounts of azobis(isobutyronitrile) (AIBN, initiator), CPDB, or CPDB-anchored NPs and monomeric VIm-TFSI were dissolved in DMF. The molar ratio of initiator to monomer n_I/n_M determines the chain length, and for PILgNPs, the molar ratio of initiator to chain transfer agent n_I/n_C determines the graft density (GD). The resulting mixture was degassed through a freeze−pump−thaw procedure for three times and then purged with nitrogen prior to reaction. The polymerization was initiated at 70 °C and kept for 72 h, followed by quenching with liquid nitrogen for 15 min. Products were precipitated by adding toluene as poor solvent and collected by centrifugation (8000 rpm, 10 min). The precipitate was redissolved in DMF, subsequently treated with toluene, and then subjected to centrifugation at 8000 rpm several times to remove free chains and unreacted monomer. Both PILgNPs and PIL were stored in DMF.

PILgNP Molecular Weight Determination and Characterization Methods. After the iron oxide NPs were etched by hydrochloric acid (HCl), molecular weights of PILgNPs and PIL were obtained by ^1H NMR (Varian 400 spectrometer). For the free PVIm-TFSI sample, an end-group analysis was applied using the given equation:

$$\bar{M}_n = M_M \overline{DP}_n = M_M \frac{\frac{A_M}{N_{H,M}}}{\frac{A_C}{N_{H,C}}}$$

$\bar{M}_n$ and M_M are molar masses of PIL and IL monomer, respectively. $\overline{DP}_n$ is the degree of polymerization of PILs; A_M and A_C are integration areas of the NMR peak from monomer and CPDB protons, respectively. $N_{H,M}$ and $N_{H,C}$ are the number of protons for the monomer and CPDB corresponding to the peaks of interest. In the calculation of the $\bar{M}_n$ of grafted samples, an empirically obtained apparent initiation efficiency (f_a: 0.34) was utilized.[45]

$$\bar{M}_n = M_M \frac{\frac{A_M}{N_{H,M}}}{\frac{A_C}{N_{H,C}} \times \frac{n_I}{n_C} \times f_a}$$

n_I and n_C are molar concentrations of monomer and CPDB, respectively, in this equation. The apparent efficiency f_a is defined as the efficiencies of initiation and chain transfer. During RAFT polymerization, the initiator decomposes to provide primary radicals that are subsequently captured by the chain transfer agent (CTA), resulting in the main RAFT equilibrium. The repeating chain transfer between the monomer and CTA molecules leads to chain propagation, and their molar ratio n_I/n_M determines the polymer molecular weight. The recipes for RAFT polymerization in bulk solution usually maintain the same molar amount of initiator and RAFT agent ($n_I = n_C$). The fraction of CTA molecules that participate to the reaction is merely determined by initiation efficiency, and the deviation between n_I/n_M value and degree of polymerization $\overline{DP}$ is attributed to the same initiation efficiency, which is reported to be around 0.5 for MMA polymerization in bulk-solution RAFT cases.[46] We determined the apparent efficiency to be around 0.34 for SI-RAFT from several testing reactions using MMA and IL monomers. This slight reduction is attributed to the steric hindrance experienced in SI-RAFT. Given that there are more than 300 CTA molecules anchored on single NP, it is impossible that all CTA molecules produce grafts, so an additional chain transfer efficiency coexists with initiation efficiency, and their product results in the reduced value f_a.

The molecular weight of PIL is also confirmed by mass spectrometry (MS) using a Micromass Quattro Ultima instrument (Waters, Milford, Massachusetts) equipped with an ESI source, and the result matched well with that from ^1H NMR. ACN was used as the solvent. Vapors emanating from a liquid nitrogen reservoir (AGL Welding Supply Co., Inc., Clifton, New Jersey) were used as the nebulizer, desolvation, and cone gas. Mass spectra were acquired in the positive ion mode over a range of m/z 200−1400. The ESI source conditions were conditioned at 3.03 kV capillary voltage; 30 V sampling cone; 120 °C source temperature; 200 °C desolvation gas heater temperature; 105 L/h cone gas flow rate; 463 L/h desolvation gas flow rate; and 20 μL/min sample infusion flow rate. The molecular weight is calculated by the peak value of neighbor m/z. Combining the equation of $\frac{M+n+1}{n+1} = 541.91$ and $\frac{M+n}{n} = 563.20$,

https://doi.org/10.1021/acs.macromol.3c02623
Macromolecules XXXX, XXX, XXX−XXX

Scheme 1. Synthesis Route of Monomeric VIm-TFSI, PIL, and PILgNPs

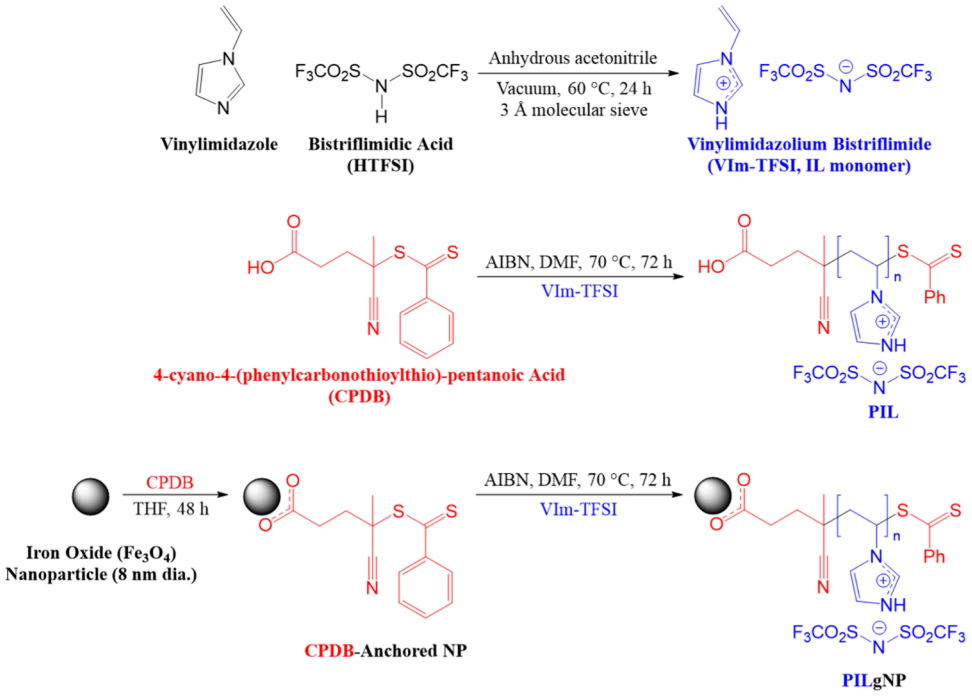

Table 1. Polymer Graft Characteristics and Hydrodynamic Sizes (R_H) of PILgNPs, Neat PIL, and CPDB-Anchored NPs Measured in *N,N*-Dimethylformamide (DMF)[a]

sample	$\bar{M}_n$ (kDa)	$\overline{DP}_n$	GD (chains/nm^2)	GD (chains/NP)	$R_{H,1}$ (nm)	$R_{H,2}$ (nm)	$R_{H,3}$ (nm)
PILgNP (HMW)	209.0	559	0.0144	2.89	19.4	50.2	
PILgNP (LMW)	93.3	249	0.0138	2.77	9.6	47.5	
PIL (neat)	15.2[b]	40.5					
CPDB-NP					7.1	19.8	102.2

[a]GD: graft density. [b]Molecular weight determined by MS.

the molecular weight of the synthesized PIL was found to be 15.20 kDa.

Using the mass of grafted chains $m_{polymer}$ and mass of NP cores m_{NP} measured by a TA Instruments Q50 thermogravimetric analyzer, the GD was calculated with the following equation.

$$GD \approx \frac{m_{polymer}}{m_{NP}} \frac{N_A \rho R}{3\bar{M}_n}$$

N_A is Avogadro's constant, ρ is the mass density of NP, R is the radius of NP core, and $\bar{M}_n$ is the number-averaged molecular weight in this equation.

Hydrodynamic sizes of NPs before and after polymerization were measured by Malvern Zetasizer Nano S. Transmission electron microscopy (JEOL 2100 Plus S/TEM) imaging was employed at 200 kV to analyze the PILgNP samples drop cast from DMF and DMF/10 vol % HMIm-TFSI solutions. Ted-Pella Lacey Carbon Type-A 300 mesh copper grids were used for the cryo-TEM sample preparation. We removed the Formvar membrane by dipping it in solvent, and the Lacey carbon film remained. For cryogenic TEM, the solution drop was frozen by liquid ethane and maintained at cryogenic temperature during the TEM imaging at 200 kV. The grids with a Formvar membrane were used for drop-cast samples for regular TEM analysis. An AC field (20 mV/cm, 100 kHz, sine wave) designed to mimic the conditions of electrochemical impedance spectroscopy (EIS), was applied to ensure that the observed morphology is stable during EIS measurements. A custom-made modular cell was constructed to apply the AC field, featuring a poly(tetrafluoroethylene) (PTFE) chamber and stainless-steel screws functioning as electrodes in eight orthogonal directions. Elemental mapping was performed by the same TEM equipped with an energy-dispersive X-ray spectroscopy system (Oxford Max-80 EDS). The data are collected and processed by Oxford INCA software.

Solution samples for SAXS were tested in borosilicate glass capillary tubes. Data was collected at ambient temperature using a Ganesha SAXSLAB instrument at Columbia University, equipped with a Cu $K\alpha$ source (λ = 1.5406 Å) and a Pilatus 300K detector with a variable sample-to-detector distance that covers the q range of 0.006−0.03 Å^{-1}.

The dielectric response of sample solutions at different ionic liquid concentrations ranging from ∼20 to ∼0.01 mM was conducted by an electrochemical impedance spectrometer (SP-300, BioLogic Science Instruments). The measurement was performed by sinusoidal AC with a 10 mV amplitude in the 7 MHz−0.1 Hz frequency range. Temperature is controlled by oil bath in the 5−70 °C range, and at each temperature, the system is allowed to stand for 5 min to reach thermal equilibrium.

RESULTS AND DISCUSSION

PIL-Grafted Nanoparticle (PILgNP) Design and Synthesis. PILgNP synthesis involves the preparation of the IL monomer, synthesis of nanoparticles, and surface initiated reversible addition−fragmentation chain transfer (SI-RAFT) polymerization steps. The detailed synthesis and purification for each step are presented in the Experimental Section (see Scheme 1). VIm-TFSI was polymerized on Fe_3O_4 NPs of 8 ± 3 nm in diameter using RAFT polymerization. Proton nuclear magnetic resonance (^{1}H NMR) was employed to determine

https://doi.org/10.1021/acs.macromol.3c02623
Macromolecules XXXX, XXX, XXX−XXX

the molecular weights of PILs (Figure S1). A modified end-group analysis is used for the PILgNPs. Samples prepared for this work are listed in Table 1. The two PILgNPs with high (209.0 kDa) and low (93.3 kDa) molecular weights of grafts are labeled as PILgNP (HMW) and PILgNP (LMW). The molecular weight of neat PIL was obtained from mass spectroscopy (MS) and ^{1}H NMR as 15.2 and 13.6 kDa, respectively.

The hydrodynamic sizes of samples were measured using dynamic light scattering (DLS) after bath sonication of the ~0.05 mg/mL samples in *N,N*-dimethylformamide (DMF). Figure 1 shows a bimodal *z*-averaged hydrodynamic size

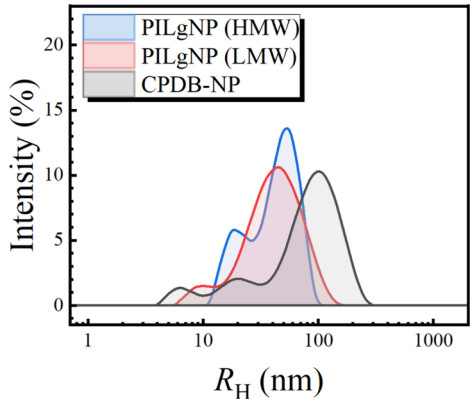

Figure 1. Hydrodynamic size (R_H) distribution of PILgNP systems and chain-transfer agent functionalized bare Fe_3O_4 nanoparticles (CPDB-NPs).

distribution of PILgNPs accounting for individual particle size ($R_{H,1}$) and small aggregates of grafted nanoparticles ($R_{H,2}$) as listed in Table 1. Bimodal distributions of sizes indicate individual grafted particles with averaged sizes $R_{H,1}$ around 19 nm for HMW and 10 nm for LMW, and cluster sizes $R_{H,2}$ around 50 and 48 nm in both PILgNPs. The number of particles in a cluster is estimated from the ratio of the two sizes. The HMW sample exhibits better dispersion and colloidal stability with $R_{H,2} = 2.6R_{H,1}$ due to its longer chain grafts than the LMW sample with $R_{H,2} = 4.7R_{H,1}$. The bare NPs (CPDB-NPs) show larger aggregates $R_{H,3}$ in solution. This simple hydrodynamic size comparison suggests that polycation chains have extended conformation compared to neutral polymers.[47]

Cryogenic TEM data of both samples at ~0.05 mg/mL concentration are conducted to show the structures in the solution state. Short strings of particles are seen for the HMW sample in both drop-cast film and frozen-state TEM data, whereas particles are more dispersed in the LMW sample (Figure 2a–d). It is important to note that samples interact with the Lacey carbon film differently. The HMW sample covers the whole grid, and the LMW sample stays on the edges of the Lacey film. Comparing the drop-cast and cryo states helped us to conclude that HMW samples form percolated strings and the LMW sample remains better dispersed in DMF. Additional cryo-TEM data is presented in Figure S4. Furthermore, TEM images were collected carefully on PILgNPs from several areas to show the continuity of nanostructures. TEM micrographs of the identical cluster are superimposed to examine the micrometer-scale dimensions of the structures. These images clearly illustrate the distinctive percolation nature of PILgNP (HMW) strings spanning micron lengths, as depicted in the TOC image and Figure S2. SAXS measurements on samples at two solution concentrations (0.5 and 5 mg/mL in DMF) were conducted using the Ganesha SAXSLAB instrument. The data was analyzed using the two-level Unified model[48,49] due to the fractal-like characteristics observed in TEM images of the

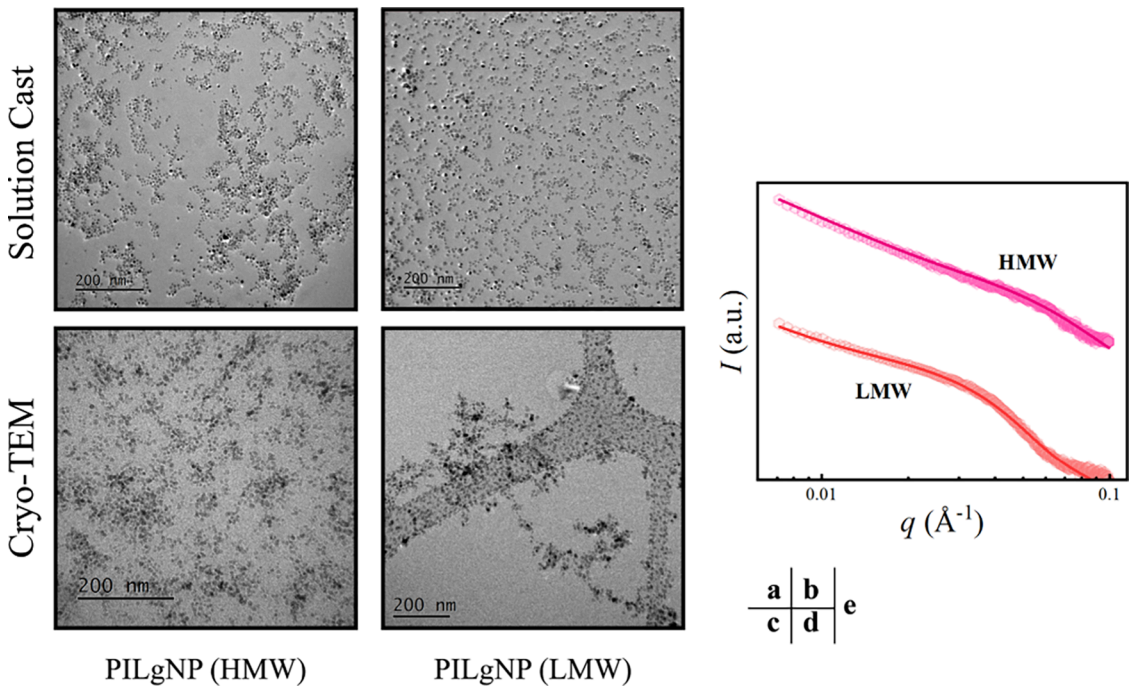

Figure 2. (a, b) TEM micrographs of solution cast PILgNP (HMW) (on the left) and PILgNP (LMW) (on the right) in DMF solution. (c, d) Cryo-TEM micrographs of samples on lacey grids. (e) SAXS profiles of PILgNP samples at 0.5 mg/mL in a DMF solution. The solid curves represent the Unified model fits to the data.

https://doi.org/10.1021/acs.macromol.3c02623
Macromolecules XXXX, XXX, XXX−XXX

Table 2. SAXS Data of Solution Samples Was Analyzed by the Unified Model Fits[a]

$$I_i(q) = G_i \exp\left(-q^2 R_{g,i}^{\frac{2}{3}}\right) + \exp\left(-q^2 R_{g,i-1}^{\frac{2}{3}}\right) B_i \operatorname{erf}\left[\frac{\left(\frac{qR_{g,i}}{\sqrt{6}}\right)^3}{q}\right]^{P_i}$$

sample	$R_{g,1}$ (Å)	B_1	G_1	P_1	$R_{g,2}$ (Å)	B_2	G_2	P_2
PILgNP (HMW)/DMF	**36.5**	1.99e−6	0.45	3.8	**372.7**	9.57e−5	57.6	2.4
PILgNP (LMW)/DMF	**67.9**	1.74e−5	76.10	4.0	**744.8**	8.13e−5	24,033	4.0

[a]The two-level fitting parameters for the primary and secondary structures are given below.

structures (Figure 2e). The fractal dimension P_1 is found to be 4 in HMW and LMW samples, and it does not change with particle concentration, indicating good colloidal stability and the similarity in structures (Figure S3). Fe_3O_4 nanoparticles of the same batch were used in preparation of the grafted nanoparticles, and the SAXS data generated 4−7 nm primary particle size listed as $R_{g,1}$ in Table 2. The secondary structure size $R_{g,2}$ is found to be 74 nm for the PILgNPs (LMW) and 37 nm for the PILgNPs (HMW), suggesting the lower polymer shielding effect with the shorter chains of PILgNP (LMW). The secondary size in LMW sample from SAXS is larger than what we observe in TEMs. This may be a result of higher solution concentration in DMF (0.5 mg/mL) for SAXS samples.

The energy-dispersive X-ray spectroscopy (TEM-EDS) data were collected to observe the local density of elements that belong to polycations and $TFSI^-$ anions. Sulfur (S) signals come from CTA in the ends of PIL chains and from the $TFSI^-$, and fluorine (F) signals are solely from $TFSI^-$ anions (Figure 3). The S signal contribution is relatively weak because each

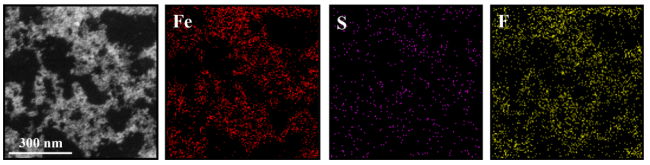

Figure 3. TEM-EDS elemental maps recorded using Fe, S, and F signals obtained from PILgNP (HMW).

$TFSI^-$ contains two S but six F atoms. The high density of $TFSI^-$ anions localized around PILs gives rise to strong F signals that match to that of the Fe_3O_4 particle cores. The data clearly support the strong affinity between polycation chains and anions and the ordering of $TFSI^-$ at large length scales following the NP nanostructures. Therefore, when PILgNPs self-assemble, the distribution of $TFSI^-$ adopts the same structure.

To ensure that structures do not evolve during impedance measurements, we applied AC fields at the same magnitude (20 mV/cm, 100 kHz) to sample solutions and examined structures in TEM. PILgNPs, whether with high and low molecular weights, exhibit consistent dispersity and maintain well-defined nanostrings (Figure S5). We built a modular Teflon cell to apply electric fields to solutions with stainless-steel electrodes positioned at different angles (Figure S6a). When DC fields higher than 16 V were applied, the accumulation of particles near one electrode was observed (Figure S6c). This phenomenon occurs because the DC input establishes a stable field gradient that possibly disrupts the percolated network. Contrastingly, sample solutions did not show any macroscopic movement of particles toward the electrodes at high AC frequency (Figure S6b).

Dynamic Measurements, Ionic Conductivity, and Ion Channeling. We designed the new PILgNP systems to showcase how the ion transport dynamics are influenced by the grafted chains. Moreover, our objective was to demonstrate that the ionic conductivity is contingent on the nanoparticle assembly. Real (resistance) Z' and imaginary (reactance) parts Z'' of impedance are attained from EIS measurement for the PILgNPs, neat PIL, and monomeric IL. Tests are conducted on solutions at varying concentrations 0.1−15 mg/mL and between 5 and 70 °C. The dissipation factor, $\tan\delta = \frac{Z'}{Z''}$, and conductivity $\sigma' = \frac{Z'}{k[(Z)'^2 + (Z'')^2]}$ are calculated from the measured data and shown in Figure 4a. The measured impedance values were used to calculate ε' and ε'' using the equations given in Supporting Information, and ε' and ε'' are plotted in Figure 4a. The cell geometric constant k is determined using KCl standard solution whose conductivity is 1412 μS/cm at 25 °C. The tan δ curves were fit by the Debye relaxation model $\tan\delta = \frac{2\pi f\tau_{EP}}{1 + (2\pi f)^2\tau_\sigma\tau_{EP}}$ to deduce the characteristic times of electrode polarization τ_{EP} and conduction τ_σ. The frequency at which the dissipation factor reaches its maximum, termed $f_{\tan\delta} = [2\pi(\tau_{EP}\tau_\sigma)^{1/2}]^{-1}$, corresponds to the reciprocal of the geometric average of these two characteristic times. The dielectric response can be divided into three ranges of frequency based on the reciprocal characteristic times, $f_{EP} = (2\pi\tau_{EP})^{-1}$ and $f_\sigma = (2\pi\tau_\sigma)^{-1}$, as marked in the conductivity profile. In the low-frequency region below f_{EP}, the temporal interval is longer than τ_{EP}, allowing ions to migrate and get trapped by electrodes.[50] This migration gives rise to polarization effects, causing a reduction in the number of available charge carriers and partially compensating for the external field. Consequently, this leads to a decrease in conductivity.[51−53] Within the intermediate-frequency range between f_{EP} and f_σ, the conductivity is predominantly dictated by the motion of the ions, resulting in a plateau in the conductivity profile. At higher frequencies exceeding f_σ, ions locally vibrate, contributing to the AC conductivity.

The molar conductivities Λ were calculated by $\Lambda = \sigma'_{ion}/C_{IL}$ to eliminate the significant impact of ion concentration variation and accentuate the structural effect. The molar IL concentrations (C_{IL}) vary in the PILgNPs, PIL, and monomeric IL (Table S2). As shown in Figure 4b, the molar conductivity Λ of neat PIL is lower than that of the IL monomer, primarily due to the reduced dynamics of the polycations. It has been shown with the simulations that anions coordinate with polycations stronger than with the free cations.[54] The sequential association and dissociation of anions to polycations give rise to ion hopping transfer, a process described by the ladder mechanism.[37,39] The PILgNP (LMW)

https://doi.org/10.1021/acs.macromol.3c02623
Macromolecules XXXX, XXX, XXX−XXX

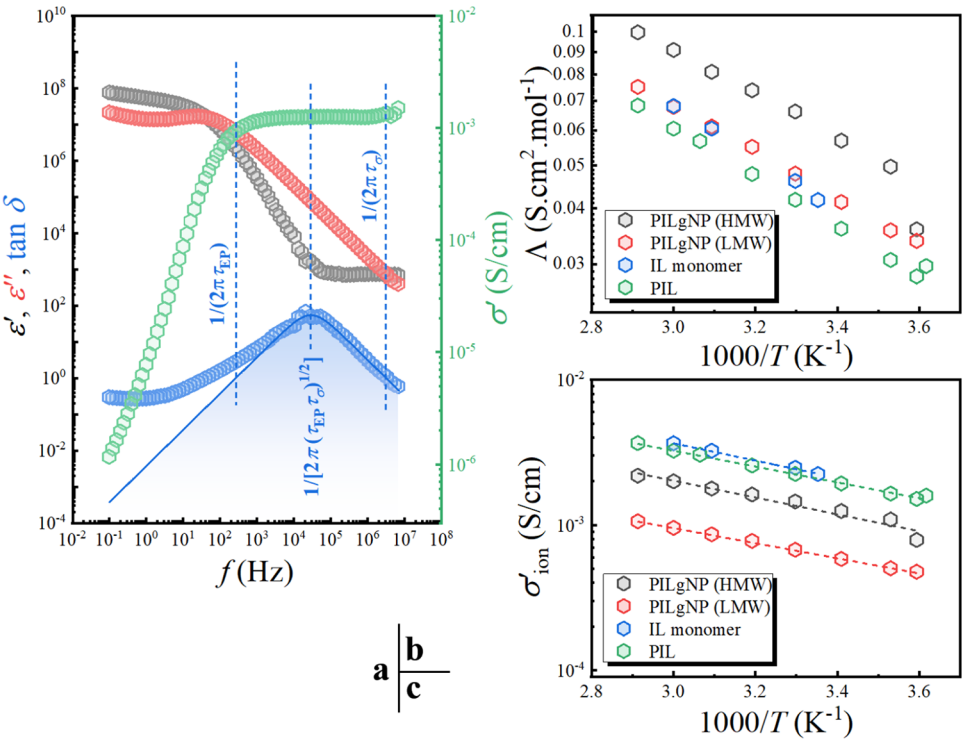

Figure 4. (a) Frequency-dependent permittivity (ε', ε'') spectra, real conductivity (σ'), and tangent loss (tan δ) of PILgNP (HMW) at 20 °C. The solid blue curve is the Debye relaxation fit to the tan δ spectrum. Arrhenius plots of (b) molar conductivities (Λ) and (c) ionic conductivities (σ'_{ion}) of PILgNP (HMW), PILgNP (LMW), neat PIL, and IL monomer. The concentration is ~15.6 mg/mL particles in DMF solution for all samples.

has higher molar conductivity (Λ) than neat PIL. This recovery of conductivity is attributed to the formation of self-assembled chains around nanoparticles that create connected pathways, namely, *ion channels*, for ionic hopping. The assembly of grafted particles establishes ionic channels that significantly enhance the ion mobility compared to that in neat PIL. The highest Λ value is measured with the PILgNPs (HMW). This rise in conductivity is a result of the improved connection of conformed PIL chains around nanostrings of particles. The anions enriched within the interstitial areas of PIL chains result in chain-like cooperative motion, thereby enhancing molar conductivity. The reduced ionic conductivity σ'_{ion} value of PILgNPs than neat PIL as observed in Figure 4c is ascribed to the grafting of polyions that restricts the cation mobility due to the conformational effect.

The ionic conductivities σ'_{ion} averaged from the intermediate-frequency plateau are measured as a function of temperature as illustrated in an Arrhenius plot (Figure 4c), so as the characteristic frequencies of electrode polarization f_{EP}, dissipation maxima $f_{tan\delta}$, and conduction relaxation f_σ (Figure S7). The activation energies are calculated from respective Arrhenius plots using the Arrhenius-form equation [e.g., $\sigma'_{ion} = \sigma_0 \exp\left(-\frac{E_{a,\sigma}}{RT}\right)$, where $E_{a,\sigma}$ is the activation energy for conduction, σ_0 is the pre-exponential factor, R is the ideal gas constant, and T is the absolute temperature. The Arrhenius behavior exhibited by all ionic conductivities and characteristic frequencies indicates a decoupled ion motion. Activation energies of dissipation factor maxima $E_{a,tan\delta}$ describe the motion of ion clusters.[8] The energies of ionic conductivity $E_{a,\sigma}$ are very close to $E_{a,tan\delta}$, suggesting that the overall ionic conductivity is dominated by the motion of ion clusters (Table 3). The activation energies of electrode polarization $E_{a,EP}$, which correspond to long-range ion migration, are significantly lower than those of the other events. The energy barrier of conduction relaxation corresponds to a single-ion motion event by cage escape, denoted as E_{a,f_σ}. Compared to polymerized counterparts, monomeric IL has higher $E_{a,tan\delta}$ and E_{a,f_σ}, ascribed to the prominent ionic clustering in IL. For neat PIL, the polymerization results in asymmetric dynamics between polycation and counteranion, alleviating ionic aggregation and reducing the associated energies of $E_{a,tan\delta}$ and E_{a,f_σ} to 10.3 and 15.3 kJ/mol, respectively. The grafting of polycations on NPs further lowers the activation energies to $E_{a,tan\delta}$: 8.5 kJ/mol and E_{a,f_σ}: 12.5 kJ/mol with the more probable single-ion motion within ionic channels, hence enhancing the conduction.

Table 3. Activation Energies of Ionic Conduction $E_{a,\sigma}$, Electrode Polarization $E_{a,EP}$, Ion Cluster Motion $E_{a,tan\delta}$, and Conduction Relaxation E_{a,f_σ} in DMF

	$E_{a,\sigma}$ (kJ/mol)	$E_{a,EP}$ (kJ/mol)	$E_{a,tan\delta}$ (kJ/mol)	E_{a,f_σ} (kJ/mol)
PILgNP (HMW)	10.3	5.1	10.2	14.6
PILgNP (LMW)	9.8	4.6	8.47	12.5
neat PIL	10.5	5.6	10.3	15.3
IL monomer	11.3	5.0	15.2	26.2

Concentration-dependent EIS data on PILgNPs, PIL, and IL monomer were measured to unveil the influence of structure on conductivity upon dilution. The critical behavior of percolation, marked by a sudden change in ionic conductivity, σ'_{ion}, is evident in PILgNP systems (Figure S8). The higher $f_{tan\delta}$ for PILgNPs after molar IL concentration (C_{IL}) correction

https://doi.org/10.1021/acs.macromol.3c02623
Macromolecules XXXX, XXX, XXX−XXX

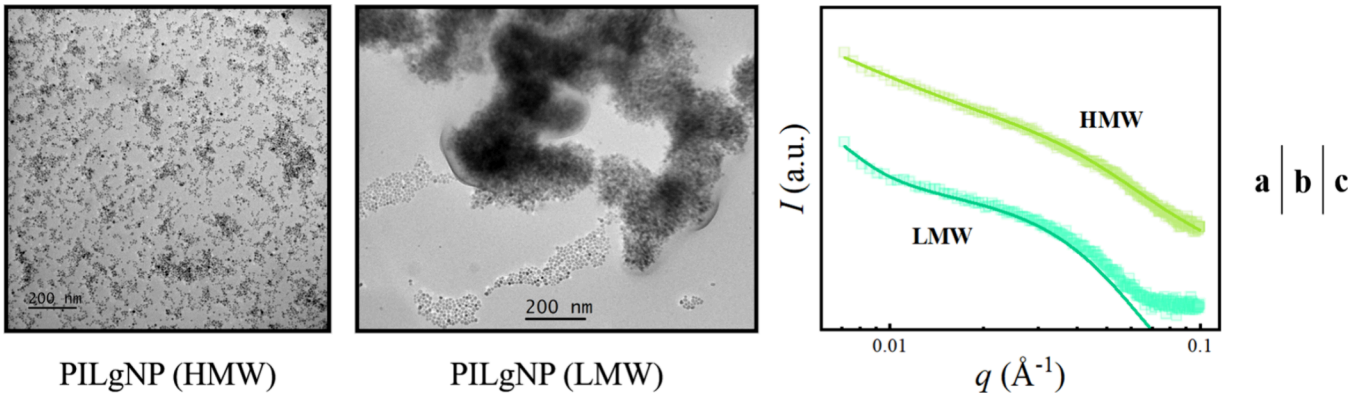

Figure 5. TEMs of (a) PILgNP (HMW) and (b) PILgNP (LMW) in HMIm-TFSI. (c) SAXS profiles of PILgNP samples in DMF/HMIm-TFSI solutions at 0.5 mg/mL concentrations. The lines represent the Unified model function fits to the data.

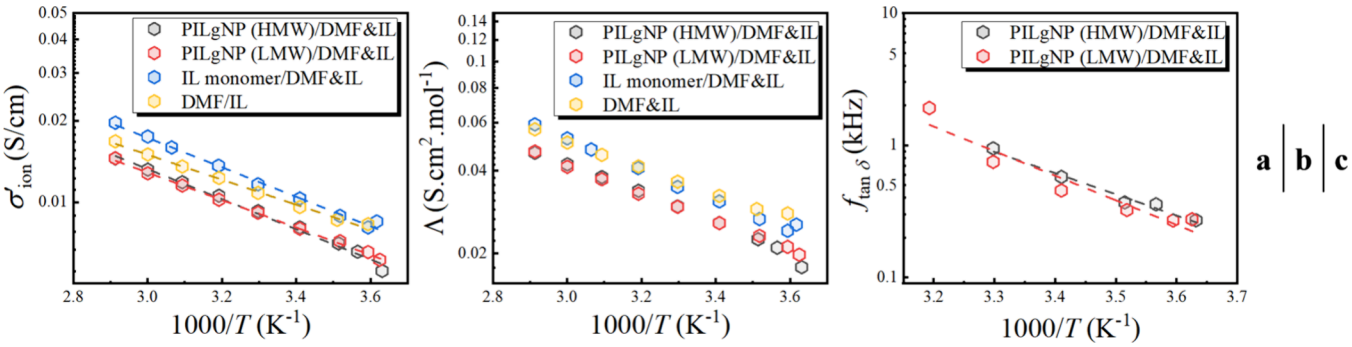

Figure 6. Arrhenius plots of (a) ionic conductivity (σ'_{ion}), (b) molar conductivity (Λ), and (c) characteristic frequency of tan δ maxima of samples in DMF/HMIm-TFSI (10 vol %).

verifies the enhanced ion mobility of PILgNPs compared to that in neat PIL (Figure S8b). The similar percolation effect is also seen in the characteristic frequencies of electrode polarization f_{EP} and conduction relaxation f_{σ}, suggesting that the ion dynamics is boosted in multiple length scales. It is important to note that $f_{\tan\delta}$ for neat PIL does not increase exponentially but rather linearly with C_{IL}.

Next, we introduced the free IL (HMIm-TFSI) to our PILgNP samples to demonstrate that the ion agglomeration and electrostatic shielding of polycation with an excess amount of $TFSI^-$ would decelerate the ionic dynamics. As shown in Figure 5, the IL addition did not change the string morphology when grafted polyelectrolyte chains are long; however, the aggregation was seen with the short polyelectrolyte chains with IL. This aggregation was also observed with the turbid solution of the PILgNP (LMW) sample (Figure S9). Ion conductivities σ'_{ion}, molar conductivities Λ, and dissipation maxima frequencies $f_{\tan\delta}$ were measured at varying temperatures (Figure 6). Table 4 shows the activation energies of the samples. The $E_{a,\tan\delta}$ values for monomeric IL and DMF/HMIm-TFSI are not attained due to their fast ion motion where ions are well solvated, so the tan δ peaks cannot be captured within the instrument's frequency range. The two PILgNPs displayed similar ion conductivity σ'_{ion} (Figure 6a) and molar conductivities Λ (Figure 6b) that are lower than those of the monomeric IL with the addition of HMIm-TFSI. Consequently, the PILgNPs cease to function as single-ion conductors. Particle structures are shown to play a minor role in ionic conductivity; thus, other proposed ion transport mechanisms such as ladder mechanism, chain-like cooperative ion motion, and Grotthuss mechanism become insignificant with the HMIm-TFSI addition. $E_{a,\sigma}$ is unchanged before and after including HMIm-TFSI while that of maxima of dissipation factor $E_{a,\tan\delta}$ jumped to ~30 kJ/mol, close to the value reported for pure HMIm-TFSI, indicative of severe ion caging.[8] Given the linear temperature dependence of σ'_{ion} and Λ (Arrhenius behavior), the dominating conduction mechanism with IL inclusion is inferred to be vehicular diffusion.

Table 4. Activation Energies of Ionic Conductivity and Dissipation Factor of All Samples in DMF/HMIm-TFSI (10 vol%) Systems

	$E_{a,\sigma}$ (kJ/mol)	$E_{a,\tan\delta}$ (kJ/mol)
PILgNP (HMW)	10.30	32.70
PILgNP (LMW)	9.80	28.70
IL monomer	10.60	
DMF/HMIm-TFSI (10 vol%)	9.01	

In summary, PILgNPs in DMF act as single-ion conductors with robust string morphology sustained with long-range electrostatic (Coulombic) interactions. The combination of particle percolation and the connection of PIL grafts resulted in effective ion channels for rapid ion transport. Upon incorporation of 10 vol% HMIm-TFSI, percolated structures are found to persist, but the PILgNPs no longer exhibit single-ion conduction. Ionic conductivity becomes independent of the chain length with the HMIm-TFSI inclusion. The ion aggregation in these systems lowers the ionic conductivity in comparison with the IL monomer.

https://doi.org/10.1021/acs.macromol.3c02623
Macromolecules XXXX, XXX, XXX−XXX

CONCLUSIONS

Two batches of PVIm-TFSI-grafted iron oxide (Fe_3O_4) NPs were synthesized at different chain lengths, and their structures and ion conductivities were investigated in DMF solutions. PIL-grafted NPs form nanostrings that readily create percolated networks at low concentrations. The structures are stabilized by the long-range electrostatic interactions, especially prevalent for the long graft chain lengths. TEM images, coupled with the critical behavior of percolation unveiled by EIS, indicate that the interstitial areas between NPs in percolated strings along with adjacent anion-enriched domains form ion channels that facilitate fast ion migration. By comparing the impedance data of the hybrids with neat poly(ionic liquid) and IL monomer, we concluded that decoupled ion transport from segmental dynamics of poly(ionic liquid)s becomes more effective when polyions are conformed. The enhanced ion conductivity, dynamics, and reduced energy barriers were elucidated by the ladder-like hopping transport of anions and chain-like cooperative ion motion within the underlying structures of PILgNPs. This is the first experimental polyelectrolyte system showcasing enhanced ion transport dynamics through the confinement created between PILgNPs. Structure-controlled ion conduction observed in new PIL-based nanohybrids holds potential applications in membrane separation technologies and energy storage devices.

ASSOCIATED CONTENT

Supporting Information

The Supporting Information is available free of charge at https://pubs.acs.org/doi/10.1021/acs.macromol.3c02623.

NMR spectra of PILgNPs and neat PIL; panoramic TEMs; SAXS data of PILgNPs at different solution concentrations; TEM images of AC field applied PILgNP solutions; photos of the modular cell for field application; Arrhenius plots of PILgNPs in solution; concentration-dependent conductivities and characteristic frequencies ($f_{\tan\delta}$, f_{EP}, f_{σ}); photos of PILgNP solutions in DMF and DMF/HMIm-TFSI; and ionic liquid concentrations C_{IL} in PILgNP samples (PDF)

AUTHOR INFORMATION

Corresponding Author

Pinar Akcora − *Department of Chemical Engineering and Materials Science, Stevens Institute of Technology Hoboken, Hoboken, New Jersey 07030, United States;* orcid.org/0000-0001-7853-7201; Email: pakcora@stevens.edu

Authors

Ruhao Li − *Department of Chemical Engineering and Materials Science, Stevens Institute of Technology Hoboken, Hoboken, New Jersey 07030, United States;* orcid.org/0000-0002-5417-4490

Deniz Bulucu − *Department of Chemistry, Brandeis University, Waltham, Massachusetts 02453, United States*

Tsengming Chou − *Department of Chemical Engineering and Materials Science, Stevens Institute of Technology Hoboken, Hoboken, New Jersey 07030, United States*

Complete contact information is available at: https://pubs.acs.org/10.1021/acs.macromol.3c02623

Author Contributions

The manuscript was written through contributions of all authors.

Notes

The authors declare no competing financial interest.

ACKNOWLEDGMENTS

We gratefully acknowledge NSF DMR TMRP Polymers award #2104924 for the financial support. D.B. was supported by NSF REU Site award #2050921. Additionally, we thank Nico Mendez for helping us with the SAXS measurements at Columbia University.

REFERENCES

(1) Diederichsen, K. M.; Buss, H. G.; McCloskey, B. D. The Compensation Effect in the Vogel-Tammann-Fulcher (VTF) Equation for Polymer-Based Electrolytes. *Macromolecules* **2017**, *50* (10), 3831−3840.

(2) Doyle, M.; Fuller, T. F.; Newman, J. The importance of the lithium ion transference number in lithium/polymer cells. *Electrochim. Acta* **1994**, *39* (13), 2073−2081.

(3) Dou, S.; Zhang, S.; Klein, R. J.; Runt, J.; Colby, R. H. Synthesis and characterization of poly(ethylene glycol)-based single-ion conductors. *Chem. Mater.* **2006**, *18* (18), 4288−4295.

(4) Fragiadakis, D.; Dou, S.; Colby, R. H.; Runt, J. Molecular mobility and Li+ conduction in polyester copolymer ionomers based on poly(ethylene oxide). *J. Chem. Phys.* **2009**, *130* (6), 064907.

(5) Zhang, S.; Dou, S.; Colby, R. H.; Runt, J. Glass transition and ionic conduction in plasticized and doped ionomers. *J. Non-Cryst. Solids* **2005**, *351* (33−36SPEC. ISS.), 2825−2830.

(6) Keith, J. R.; Rebello, N. J.; Cowen, B. J.; Ganesan, V. Influence of Counterion Structure on Conductivity of Polymerized Ionic Liquids. *ACS Macro Lett.* **2019**, *8* (4), 387−392.

(7) Shen, K. H.; Hall, L. M. Effects of ion size and dielectric constant on ion transport and transference number in polymer electrolytes. *Macromolecules* **2020**, *53* (22), 10086−10096.

(8) Li, R.; Feng, Y.; Akcora, P. Examining ionicity and conductivity in poly(methyl methacrylate) containing imidazolium-based ionic liquids. *J. Mol. Liq.* **2023**, *382*, No. 121897.

(9) Liu, S.; Walton, M.; Tarakina, N. V.; Akcora, P. Solvation in Ionic Liquids with Polymer-Grafted Nanoparticles. *J. Phys. Chem. B* **2020**, *124* (23), 4843−4850.

(10) Liu, S.; Tyagi, M.; Akcora, P. Polymer-coupled local dynamics enhances conductivity of ionic liquids. *Macromolecules* **2020**, *53* (15), 6538−6546.

(11) Liu, S.; Liedel, C.; Tarakina, N. V.; Osti, N. C.; Akcora, P. Dynamics of ionic liquids in the presence of polymer-grafted nanoparticles. *Nanoscale* **2019**, *11* (42), 19832−19841.

(12) Liu, S.; Li, R.; Tyagi, M.; Akcora, P. Confinement Effects in Dynamics of Ionic Liquids with Polymer-Grafted Nanoparticles. *ChemPhysChem* **2022**, *23* (18), No. e202200219.

(13) Tröger-Müller, S.; Antonietti, M.; Liedel, C. Stability of the zwitterionic liquid butyl-methyl-imidazol-2-ylidene borane. *Phys. Chem. Chem. Phys.* **2018**, *20* (16), 11437−11443.

(14) Kim, O.; Kim, S. Y.; Park, B.; Hwang, W.; Park, M. J. Factors Affecting Electromechanical Properties of Ionic Polymer Actuators Based on Ionic Liquid-Containing Sulfonated Block Copolymers. *Macromolecules* **2014**, *47* (13), 4357−4368.

(15) Zhang, J.; Chen, Z.; Zhang, Y.; Dong, S.; Chen, Y.; Zhang, S. Poly(ionic liquid)s Containing Alkoxy Chains and Bis(trifluoromethanesulfonyl)imide Anions as Highly Adhesive Materials. *Adv. Mater.* **2021**, *33* (30), 2100962.

(16) Nürnberg, P.; Atik, J.; Borodin, O.; Winter, M.; Paillard, E.; Schönhoff, M. Superionicity in Ionic-Liquid-Based Electrolytes Induced by Positive ion−ion Correlations. *J. Am. Chem. Soc.* **2022**, *144* (10), 4657−4666.

(17) Neale, A. R.; Murphy, S.; Goodrich, P.; Hardacre, C.; Jacquemin, J. Thermophysical and Electrochemical Properties of Ethereal Functionalised Cyclic Alkylammonium-based Ionic Liquids as Potential Electrolytes for Electrochemical Applications. *ChemPhysChem* **2017**, *18* (15), 2040−2057.
(18) Paren, B. A.; Nguyen, N.; Ballance, V.; Hallinan, D. T.; Kennemur, J. G.; Winey, K. I. Superionic Li-Ion Transport in a Single-Ion Conducting Polymer Blend Electrolyte. *Macromolecules* **2022**, *55* (11), 4692−4702.
(19) Tamilarasan, P.; Ramaprabhu, S. Stretchable supercapacitors based on highly stretchable ionic liquid incorporated polymer electrolyte. *Mater. Chem. Phys.* **2014**, *148* (1), 48−56.
(20) Shabeeba, P.; Thayyil, M. S.; Pillai, M. P.; Thasneema, K.K. PMMA-RTIL electrolyte for high-energy supercapacitors: A comparison of different anions. *J. Mol. Liq.* **2019**, *294*, No. 111671.
(21) Jamil, R.; Silvester, D. S. Ionic liquid gel polymer electrolytes for flexible supercapacitors: Challenges and prospects. *Current Opinion in Electrochemistry* **2022**, *35*, No. 101046.
(22) He, Q.; Vokoun, D.; Stalbaum, T.; Kim, K. J.; Fedorchenko, A. I.; Zhou, X.; Yu, M.; Dai, Z. Mechanoelectric transduction of ionic polymer-graphene composite sensor with ionic liquid as electrolyte. *Sensors and Actuators A: Physical* **2019**, *286*, 68−77.
(23) Kim, O.; Kim, H.; Choi, U. H.; Park, M. J. One-volt-driven superfast polymer actuators based on single-ion conductors. *Nat. Commun.* **2016**, *7* (1), 13576.
(24) Zhao, Q.; Heyda, J.; Dzubiella, J.; Täuber, K.; Dunlop, J. W. C.; Yuan, J. Sensing Solvents with Ultrasensitive Porous Poly(ionic liquid) Actuators. *Adv. Mater.* **2015**, *27* (18), 2913−2917.
(25) Wei, P.; Pan, X.; Chen, C. Y.; Li, H. Y.; Yan, X.; Li, C.; Chu, Y. H.; Yan, B. Emerging impacts of ionic liquids on eco-environmental safety and human health. *Chem. Soc. Rev.* **2021**, *50* (24), 13609−13627.
(26) Sha, M.; Ma, X.; Li, N.; Luo, F.; Zhu, G.; Fayer, M. D. Dynamical properties of a room temperature ionic liquid: Using molecular dynamics simulations to implement a dynamic ion cage model. *J. Chem. Phys.* **2019**, *151* (15), 154502.
(27) Le Bideau, J.; Viau, L.; Vioux, A. Ionogels, ionic liquid based hybrid materials. *Chem. Soc. Rev.* **2011**, *40* (2), 907−925.
(28) Stacy, E. W.; Gainaru, C. P.; Gobet, M.; Wojnarowska, Z.; Bocharova, V.; Greenbaum, S. G.; Sokolov, A. P. Fundamental Limitations of Ionic Conductivity in Polymerized Ionic Liquids. *Macromolecules* **2018**, *51* (21), 8637−8645.
(29) Lall-Ramnarine, S. I.; Zhao, M.; Rodriguez, C.; Fernandez, R.; Zmich, N.; Fernandez, E. D.; Dhiman, S. B.; Castner, E. W.; Wishart, J. F. In *Connecting Structural and Transport Properties of Ionic Liquids with Cationic Oligoether Chains*. *J. Electrochem. Soc.* **2017**, *164*, H5247−H5262.
(30) Kinsey, T.; Glynn, K.; Cosby, T.; Iacob, C.; Sangoro, J. Ion Dynamics of Monomeric Ionic Liquids Polymerized in Situ within Silica Nanopores. *ACS Appl. Mater. Interfaces* **2020**, *12* (39), 44325−44334.
(31) Nishimura, N.; Ohno, H. 15th anniversary of polymerised ionic liquids. *Polymer* **2014**, *55* (16), 3289−3297.
(32) Cowan, M. G.; Gin, D. L.; Noble, R. D. Poly(ionic liquid)/Ionic Liquid Ion-Gels with High "free" Ionic Liquid Content: Platform Membrane Materials for CO2/Light Gas Separations. *Acc. Chem. Res.* **2016**, *49* (4), 724−732.
(33) Zhao, Q.; Fellinger, T. P.; Antonietti, M.; Yuan, J. Nitrogen-doped carbon capsules via poly(ionic liquid)-based layer-by-layer assembly. *Macromol. Rapid Commun.* **2012**, *33* (13), 1149−1153.
(34) Zhao, Q.; Zhang, P.; Antonietti, M.; Yuan, J. Poly(ionic liquid) complex with spontaneous micro-/mesoporosity: Template-free synthesis and application as catalyst support. *J. Am. Chem. Soc.* **2012**, *134* (29), 11852−11855.
(35) Maksym, P.; Tarnacka, M.; Dzienia, A.; Erfurt, K.; Chrobok, A.; Zięba, A.; Wolnica, K.; Kaminski, K.; Paluch, M. A facile route to well-defined imidazolium-based poly(ionic liquid)s of enhanced conductivity: Via RAFT. *Polym. Chem.* **2017**, *8* (35), 5433−5443.
(36) Koyilapu, R.; Singha, S.; Kutcherlapati, S. N. R.; Jana, T. Grafting of vinylimidazolium-type poly(ionic liquid) on silica nanoparticle through RAFT polymerization for constructing nanocomposite based PEM. *Polymer* **2020**, *195*, 399.
(37) Keith, J. R.; Mogurampelly, S.; Aldukhi, F.; Wheatle, B. K.; Ganesan, V. Influence of molecular weight on ion-transport properties of polymeric ionic liquids. *Phys. Chem. Chem. Phys.* **2017**, *19* (43), 29134−29145.
(38) Zhang, Z.; Zofchak, E.; Krajniak, J.; Ganesan, V. Influence of Polarizability on the Structure, Dynamic Characteristics, and Ion-Transport Mechanisms in Polymeric Ionic Liquids. *J. Phys. Chem. B* **2022**, *126* (13), 2583−2592.
(39) Mogurampelly, S.; Keith, J. R.; Ganesan, V. Mechanisms Underlying Ion Transport in Polymerized Ionic Liquids. *J. Am. Chem. Soc.* **2017**, *139* (28), 9511−9514.
(40) Li, R.; Han, Y.; Akcora, P. Ion channels in sulfonated copolymer-grafted nanoparticles in ionic liquids. *Soft Matter* **2022**, *18* (29), 5402−5409.
(41) Fan, M.; Shen, K.-H.; Hall, L. M. Effect of Tethering Anions in Block Copolymer Electrolytes via Molecular Dynamics Simulations. *Macromolecules* **2022**, *55* (17), 7945−7955.
(42) Kim, O.; Kim, s. y.; Ahn, H.; Kim, C.; Rhee, Y.; Park, M. J. Phase Behavior and Conductivity of Sulfonated Block Copolymers Containing Heterocyclic Diazole-Based Ionic Liquids. *Macromolecules* **2012**, *45*, 8702−8713.
(43) Zhao, W.; Sun, J. Triflimide (HNTf2) in Organic Synthesis. *Chem. Rev.* **2018**, *118* (20), 10349−10392.
(44) Gnahm, M.; Kolb, D. M. The purification of an ionic liquid. *J. Electroanal. Chem.* **2011**, *651* (2), 250−252.
(45) Favier, A.; Charreyre, M.-T. Experimental Requirements for an Efficient Control of Free-Radical Polymerizations via the Reversible Addition-Fragmentation Chain Transfer (RAFT) Process. *Macromol. Rapid Commun.* **2006**, *27* (9), 653−692.
(46) Perrier, S. 50th Anniversary Perspective: RAFT Polymerization—A User Guide. *Macromolecules* **2017**, *50* (19), 7433−7447.
(47) Han, A.; Uppala, V. V. S.; Parisi, D.; George, C.; Dixon, B. J.; Ayala, C. D.; Li, X.; Madsen, L. A.; Colby, R. H. Determining the Molecular Weight of Polyelectrolytes Using the Rouse Scaling Theory for Salt-Free Semidilute Unentangled Solutions. *Macromolecules* **2022**, *55* (16), 7148−7160.
(48) Beaucage, G. Approximations Leading to a Unified Exponential/Power-Law Approach to Small-Angle Scattering. *J. Appl. Crystallogr.* **1995**, *28* (6), 717−728.
(49) Beaucage, G. In *Combined Small-Angle Scattering for Characterization of Hierarchically Structured Polymer Systems over Nano-to-Micron Meter: Part II Theory*; Elsevier 2012.
(50) Sitaputra, W.; Stacchiola, D.; Wishart, J. F.; Wang, F.; Sadowski, J. T. In Situ Probing of Ion Ordering at an Electrified Ionic Liquid/Au Interface. *Adv. Mater.* **2017**, *29* (27), 1606357.
(51) Choi, U. H.; Lee, M.; Wang, S.; Liu, W.; Winey, K. I.; Gibson, H. W.; Colby, R. H. Ionic Conduction and Dielectric Response of Poly(imidazolium acrylate) Ionomers. *Macromolecules* **2012**, *45* (9), 3974−3985.
(52) Singh, P.; Bharati, D. C.; Kumar, H.; Saroj, A. L. Ion transport mechanism and dielectric relaxation behavior of PVA-imidazolium ionic liquid-based polymer electrolytes. *Phys. Scr.* **2019**, *94* (10), 105801.
(53) Verma, H.; Mishra, K.; Rai, D. K. Microporous PVDF−PMMA Blend-Based Gel Polymer Electrolyte for Electrochemical Applications: Effect of PMMA on Electrochemical and Structural Properties. *J. Electron. Mater.* **2022**, *51* (2), 635−651.
(54) Mogurampelly, S.; Ganesan, V. Ion Transport in Polymerized Ionic Liquid−Ionic Liquid Blends. *Macromolecules* **2018**, *51* (23), 9471−9483.

https://doi.org/10.1021/acs.macromol.3c02623
Macromolecules XXXX, XXX, XXX−XXX